Ab initio study of polarizability and induced charge densities in multilayer graphene films

E. K. Yu*
Department of Electrical and Computer Engineering, Cornell University, Ithaca, New York 14853, USA

D. A. Stewart†
Cornell Nanoscale Facility, Cornell University, Ithaca, New York 14853, USA

S. Tiwari
Department of Electrical and Computing Engineering, Cornell University, Ithaca, New York 14853, USA

(Received 20 September 2007; revised manuscript received 8 April 2008; published 6 May 2008)

We present an *ab initio* analysis of polarization of multilayer graphene systems under applied electric fields. The effects of applied electric fields are calculated using a Berry phase approach within a plane-wave density functional formalism. We have determined polarizability values for graphene films and carbon nanotubes and found that the polarizability of graphene films follows a linear relationship with the number of layers. We also examined changes in the induced charge distribution as a function of graphene layers. We focus, in particular, on the bilayer graphene system. Under applied electric fields, we found the *Mexican hat* band structure near the *K* point reported by previous groups. We found that the induced charge primarily accumulated on the *B* sublattice sites. This observation is supported by additional calculations with a tight-binding Green's function model. By examining the local density of states at the Fermi energy, we found a high density of states at the *B* sites at the Fermi energy. In contrast, coupling between *A* sites in neighboring graphene layers leads to negligible density of states at the Fermi level. This high density of states at the *B* sites results in greater induced charge under applied electric fields. This scenario of preferential induced charge on the *B* sublattice sites under applied electric fields could impact the stability of atoms and molecules absorbed on bilayer graphene.

DOI: 10.1103/PhysRevB.77.195406 PACS number(s): 81.05.Uw, 71.15.Mb, 77.22.Ej

I. INTRODUCTION

Nanoscale forms of carbon such as nanotubes, fullerenes, and graphene have a variety of electronic and mechanical properties that have generated intense interest. Carbon nanotubes have been used to develop a number of nanoscale devices.[1] However, the ability to isolate specific metallic and semiconducting nanotubes has been difficult and has served as an impediment to mass production of nanotube devices. Single layer graphene sheets have recently been isolated and have provided an interesting alternative basis for carbon electronics.[2] Graphene has been used as a metallic channel field effect transistor.[3] Graphene charge carrier concentrations can be continuously adjusted with a gate voltage[4] between hole and electron concentrations of 10^{13} cm^{-2}. A recent paper also found that high room temperature mobilities around 200 000 $cm^2/V\,s$ are possible for technologically relevant carrier concentrations.[5] In addition, recent studies of bilayer graphene have shown that an applied electric field or dopants can induce a band gap.[6] These unique features, coupled with the fact that multilayer graphene can be grown and patterned on SiC, provide an important foundation for graphene based electronics.[7]

The discovery that an applied electric field induces a band gap in bilayer graphene[6] has generated great interest in the effects of external fields on graphene structures. McCann[8] developed a tight-binding model for bilayer graphene and found a linear relationship between the induced band gaps and induced charges in the bilayer. Guinea *et al.*[9] used a tight-binding Green's function approach to look at graphene films under an applied electric field. They found that the applied field induced quasi-one-dimensional (1D) van Hove singularities in the density of states. They also found that the carbon atoms in graphene surface with nearest neighbors in the adjacent layers have a negligible density of states at the Fermi energy.[9] Min *et al.*[10] also examined the effect of electric fields on graphene bilayers using a density functional approach. These calculations found the characteristic *Mexican hat* band diagram under an applied field predicted by tight-binding models. They also found that the band gap saturated at a value of 0.25 eV with applied field.

In this work, we examine the properties of graphene multilayers and graphite under an applied electric field by using a first-principles density functional approach. Since graphene structures can now be grown with single layer precision, it is important to study the transition to bulklike behavior. We determine the polarizability for different graphene systems and use this to estimate the dielectric constant for bulk graphite. In addition, we examine the charge distribution induced by the applied electric field and the effects on the band structure. Additional calculations with a tight-binding Green's function approach are also done to understand the formation of induced charge in bilayer graphene under applied electric fields.

II. APPROACH

Graphene consists of a honeycomb lattice of carbon atoms made up of two inequivalent triangular sublattices of *A* and *B* carbon sites (Fig. 1). The carbon atoms are linked by sp^2 bonds where the bond distance is 1.418 Å. Coupling between remaining p_z orbitals at each atom leads to the π valence and conduction bands near the Fermi energy that domi-

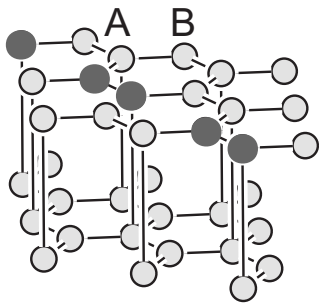

FIG. 1. Two layers of graphite are shown. Graphene sheets consist of two inequivalent sites *A* and *B*. The *A* sites have neighboring *A* sites in the layers directly above and below. The dark gray atoms in the upper layer are used to denote the direction along, which the charge density cross-sections are taken in Fig. 7.

nate transport in graphene. For all structures, we assume that the graphene layers follow Bernal stacking ($ABAB\cdots$) in the same fashion as bulk graphite. The distance between graphene layers is given by 3.347 Å. The *A* site carbon atoms have nearest neighbors directly above and below them in the neighboring graphene layers.

For our investigation, we performed first-principles calculations of carbon nanotube and graphene systems by using a density functional approach with pseudopotentials and a plane wave basis set within the local density approximation (LDA) implemented in the ABINIT package.[11,12] We used norm-conserving Troullier–Martins pseudopotentials for the carbon atoms.[13]

While density functional theory, in principle, can provide the correct charge density and ground state energy for any system, in practice, it has difficulties describing long range van der Waals interactions within the commonly used LDA or generalized gradient approximation (GGA) for the exchange and correlation energies. By using the LDA density functional approach, Schabel and Martins[14] found good agreement with experimental values for interlayer spacing and binding energy in graphite. They also compared the LDA density functional potential for graphene-graphene layer interactions to an empirical potential that included van der Waals interactions. The two potentials were found to match for distances around the equilibrium interlayer distance. Girifalco and Hodak[15] surveyed several density functional calculations that are performed on graphitic structures and found that DFT-LDA calculations were accurate for separation distances less than 1.15 that of the equilibrium separation. It should be stated that in the case of the LDA approximation, the ability to match the experimental interlayer spacing is due to a fortuitous cancellation of errors.[16] In contrast, calculations that are based on the generalized gradient approximation overestimate bond lengths and for the case of two graphene layers does not predict binding at all.[16] Using a density functional approach is also preferable to empirical approaches because it provides insight into the underlying physics in the system. Previous studies have found that the weak van der Waals bonding has little impact on graphite properties once the proper spacing between layers is fixed for calculations.[17] Since all calculations performed in this study will be done at the equilibrium graphite interlayer lattice spacing, we expect our results to be in quantitative agreement with the experiment.

Due to the fact that plane wave density functional approaches rely on a supercell geometry that is periodic in all three directions, it is important to isolate the graphene film under study from neighboring mirror images. For the supercell dimension perpendicular to the graphene plane, we did several total energy convergence tests ranging from 20 bohr (10.58 Å) to 50 bohr (26.46 Å). The results show that 30 bohr provide an acceptable balance between calculation speed and accuracy, having an energy difference less than 10^{-7} hartree between the total energies for 30 and 40 bohr of separation. Based on the work done by Konstantinova *et al.*,[18] we also used a 12×12 Monkhorst–Pack shifted two-dimensional (2D) *k*-point grid in the Brillouin zone, which provided converged total energy in terms of *k* points. An energy cutoff of 40 hartree was used for the plane-wave basis set, which was sufficient to converge the total system energy.

For homogeneous electric fields, the ABINIT code calculates the static response of insulators through a perturbation theory implementation that follows the modern theory of polarization by King-Smith and Vanderbilt.[19] In this implementation, the position operator in the perturbation term is replaced by a Berry phase expression when we consider the periodic system energy function.[20,21] Since the polarization under applied field can be expressed as a Berry phase over occupied bands, this approach can be used in a density functional formalism. For all of the systems we modeled, we applied electric fields perpendicular to the graphene film ranging from −0.0002 to 0.0002 a.u. (1 a.u. field =514.22 V/nm). The Berry phase calculation generates the polarization vectors in the Cartesian coordinates, which we use to extract polarization properties. We applied this range of electric field settings to graphene films with $N\leq7$ layers and observed the differences in charge densities and polarization. We also performed electric field calculations on (7,0) and (10,0) nanotubes and extracted corresponding properties for these systems.

The system polarization can be related to the applied electric field via $P=\chi E$, where χ is the electric susceptibility. The optical dielectric susceptibility can be derived from the slope of the polarization versus electric field graph for each system. The dielectric constant ε for the supercell can then be determined from the following equation:

$$\varepsilon = 1 + 4\pi\chi. \tag{1}$$

In order to study the variable effects of applied electric field on the band gaps of the systems, we then increased the Monkhorst–Pack 2D *k*-point grid to 30×30 for systems of one to three sheets of graphene for high resolution charge density analysis. Focusing on the graphene bilayer system, in which a controllable band gap can be introduced by applying an electric field, we increased the range of field strengths to 0.003 a.u. (1.54266 V/nm) at steps of 0.0002 and 0.0005 a.u. We also plotted the energy band diagrams near the *K* point and examined how the field influences the bands.

III. DIELECTRIC PROPERTIES

The dielectric constant for different graphene thin films was examined as a function of the number of graphene lay-

ers. The bulk dielectric constant for graphite was calculated to be 3.328 based on the Berry phase calculation. For all of the calculations within this work, the supercells were constructed to give a vacuum region of 30 bohr between the periodic images of the graphene stacks. The graphene film dielectric constant shows an almost linear relationship with the number of layers. However, repeated calculations with varying unit-cell sizes have shown that for systems such as films and nanowires, these dielectric constant values strongly depend on supercell size, an issue which has been brought up in other literature.[22,23] Since the present calculations are performed using a periodic unit cell, the calculated dielectric constant is not for an isolated stack of graphene but rather a multilayer system consisting of graphene stacks separated by 30 bohr vacuum regions. This indicates that the dielectric constant is not a good measure of polarization for these few layer graphene structures.

In order to observe the effects that adding graphene layers has on charge polarization in each system, it is more suitable to consider the polarizability α of the graphene stack under the electric field. In general terms, the polarizability defines the relationship ($\mathbf{p}_{\mathrm{loc},i}=\Sigma_j \alpha_{ij}\mathbf{E}_{\mathrm{loc},j}$) between the dipole moment $\mathbf{p}$ of the induced charge in direction i and the local electric field $\mathbf{E}_{\mathrm{loc}}$ acting in direction j. For a slab of material, we can define the polarizability of the slab in terms of $\mathbf{m}=\alpha\mathbf{E}_{\mathrm{loc}}/S$, where $\mathbf{m}$ is the electric dipole per unit surface area, the electric field $\mathbf{E}_{\mathrm{loc}}$ is perpendicular to the layers within the slab, and S is the surface unit cell for graphene.

If we consider an isolated graphene stack under an applied electric field, then the polarizability should be independent of the size of our supercell. This, in fact, holds true when the distance between the periodic graphene stacks is great enough to prevent electrostatic interactions between periodic images. The Clausius–Mossotti polarizability for an isolated slab of material can be expressed as

$$\alpha = \frac{\Omega}{4\pi}\left(\frac{\varepsilon - 1}{\varepsilon}\right), \tag{2}$$

where Ω is the supercell volume and ε is the dielectric constant in the perpendicular direction of the supercell.[22] It is important to note that the calculated dielectric constant for the supercell system is a function of the supercell volume, $\varepsilon(\Omega)$. For sufficient spacing between the periodic graphene stacks, the polarizability converges to a constant value.

For (7,0) and (10,0) carbon nanotube systems, we obtain a polarizability per unit length of 6.489 and 10.967 Å^2, respectively, when the electric field is applied perpendicular to the nanotube axis. These results are in excellent agreement with carbon nanotube polarizability values [(7,0) NT 6.47 Å^2; (10,0) NT 10.9 Å^2] obtained by Kozinsky and Marzari[23] using a different first-principles approach. For a single graphene sheet, we obtained a polarizability of 0.867 Å^3. For comparison, the polarizability for a single boron nitride sheet was calculated to be 1.32 Å^3 in a previous paper.[24] The polarizability values for graphene sheets versus the number of layers for graphene systems are shown in Fig. 2. From the plot, we see there is a linear relationship between the polarizability and the number of graphene layers, which is similar to previous works on benzene and anthracene multilayers.[22]

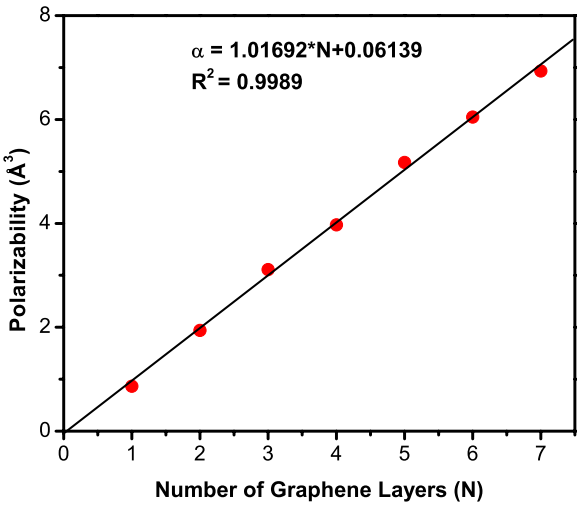

FIG. 2. (Color online) Polarizability (red circles) in graphene thin films is shown as a function of the number of layers. The linear fit to Eq. (3) is also shown.

The polarizability of a slab can be thought of as the effective volume of the slab that acts like a metal in responding to the applied electric field. From Eq. (2), we see that there are two extremes for the polarizability based on the dielectric constant. If we take $\varepsilon=1$, a slab of free space, the polarizability, or effective metallic volume is zero and no polarization occurs under the applied field. However, for the case of a metal ($\varepsilon=\infty$), we obtain the highest polarizability, $\Omega_{\mathrm{slab}}/4\pi$, and the induced surface charge density completely shields the applied electric field inside the slab. For a graphene slab, the dielectric constant within the slab is fairly constant except near the surfaces. Therefore, as we add more graphene layers, the slab volume will linearly increase and the polarizability (effective metallic volume) and charge that can respond to the field will also linearly increase. This linear relationship can also be derived by using more rigorous arguments (see Tóbik and Corso[22] for details).

We can express the slab polarizability as a function of graphene layers as

$$\alpha(N) = N\frac{\Omega_B}{8\pi}\left(\frac{\varepsilon_B - 1}{\varepsilon_B}\right) + 2\alpha_S, \tag{3}$$

where N is the number of graphene layers, Ω_B is the volume of the bulk unit cell, and α_S is the surface polarizability.[22] Fitting the polarizability data to Eq. (3), we find the slope of the line and obtain 3.68 for the bulk dielectric constant of graphite. A surface polarizability of 0.061 Å^3 for graphene thin films can also be extracted. This surface polarizability is roughly 10 times less than that of a comparable benzene film.[22]

The fitted bulk dielectric constant is slightly higher than the value 3.328 derived from the Berry phase calculation we performed for bulk graphite. This discrepancy can be traced to the underlying assumptions of the Clausius–Mossotti approach. In this framework, a solid is viewed in terms of a

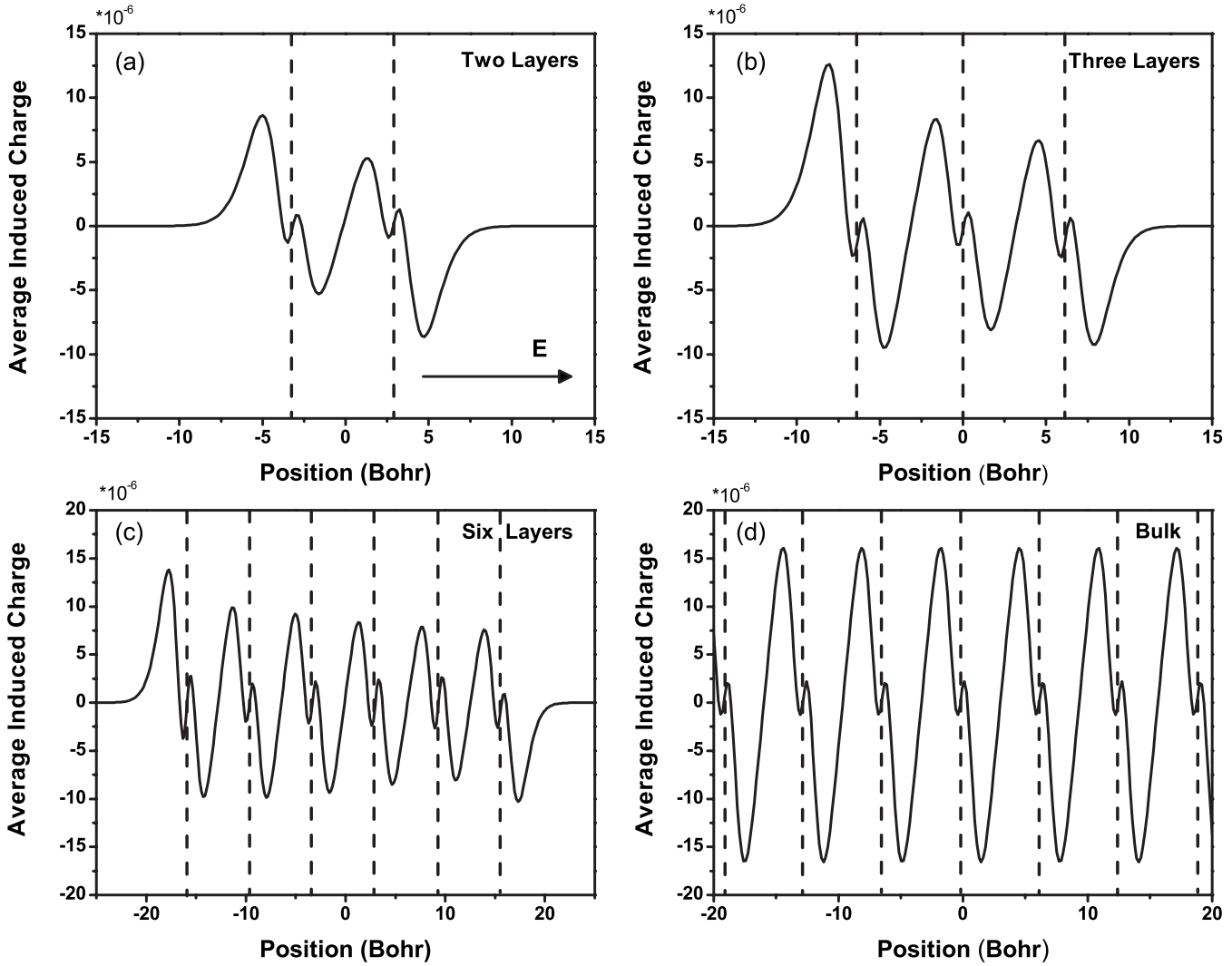

FIG. 3. The average induced charge densities in the *x-y* plane generated by an applied field of 0.1028 V/nm along the *z* axis are shown for (a) two layer, (b) three layer, and (c) six layer graphene films as well as (d) bulk graphite. The electric field in all cases is along the *z* direction. The electric field vector used in all cases is denoted in panel (a). For each plot, the origin in the *z* direction is taken as the center of the graphene film. The planes of the individual graphene layers are denoted by the dashed lines in each panel.

collection of well spaced and independent polarizable units.[25] Local dipoles are well defined in these structures. However, this local dipole model breaks down in materials where there is strong covalent bonding and delocalized electrons.

If we consider the case of graphene stacks, we have individual layers where the electrons are delocalized in the plane. Due to the 3.347 Å separation between graphene layers, neighboring layers are weakly coupled and some degree of polarization would be expected for individual layers. The slab itself is also isolated in the supercell, which will allow for charge build up at the two surfaces. The strongest coupling between layers will occur at the *A* site carbon atoms, which have adjacent *A* sites in the neighboring layers directly above and below. This coupling is not included in the Clausius–Mossotti framework and leads to the differences between the two calculated dielectric constants for bulk graphite.

We examined how the overall induced charge density profile changes as the number of graphene layers increases. To observe this transition, we subtracted the charge densities in a two dimensional *xy* plane for each carbon system in zero field from that for a field of 0.1028 V/nm. The electric field points in the positive *z* direction for all cases considered. This difference was averaged over the *xy* plane to get the variation of the charge distribution along the *z* axis. The set of graphs in Fig. 3 highlights the effects of the electric field on the average induced charge in *xy* planes and the shielding effects of these nanostructures. Since this figure plots electron charge density, positive values indicate electron accumulation and negative values indicate hole accumulation. For the discussion below, the left and right sides of each graphene film are defined as the sections with negative and positive *z* values, respectively.

In all the graphs for thin layer graphene structures, there is clear evidence for polarization with electron accumulation on the far left layer and hole accumulation on the far right layer. The induced charge profiles for all multilayer graphene structures also exhibit some degree of asymmetry. This indicates that the graphene thin film is screening a portion of the

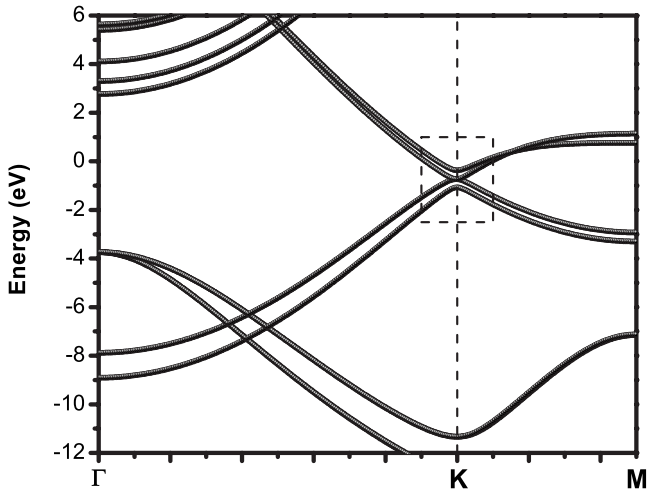

FIG. 4. The bands for a bilayer graphene system are shown along the path Γ to *K* to *M*. A dashed box around the intersection of the valence and conduction bands at the *K* point is used to denote the band region that will be considered in Fig. 5.

applied field. For the case of very poor screening, the induced charge would be identical on all layers. For the graphene bilayer, the screening is very small and the magnitude of induced charge on each layer is almost equal. For the three layer graphene film, the screening increases with a charge peak of 12.6 $\mu e^-/(\text{bohr})^3$ on the left layer and a maximum average induced charge of −9.25 $\mu e^-/(\text{bohr})^3$ on the right layer. In the case of the six layer graphene structure, the screening increases, with the average induced electron charge reaches a peak of approximately 13.8 $\mu e^-/(\text{bohr})^3$, while the right layer reaches a maximum average induced charge of only −10.3 $\mu e^-/(\text{bohr})^3$. For the different multilayer structures, the interior layers are shielded from the applied field and have a much lower induced charge.

A. Induced charge in bilayer graphene

Since bilayer graphene has the potential to play an important role in graphene based devices, we also examined the band structure and charge distribution in bilayers as a function of applied electric field. Calculating the band structure under applied electric field provides an important check of our approach. The band diagram along the path from Γ to *K* to *M* is shown in Fig. 4. It is clear that the lowest conduction band and highest valence bands intersect at the *K* point. The region that is enclosed in the dashed box in Fig. 4 is shown in Fig. 5 for the case of no applied field and applied fields ranging up to 1.5426 V/nm. For the case where there is no applied field, a conduction and valence band intersect at the *K* point, which is similar to what occurs in single layer graphene.

Upon applying a small electric field (E=0.5412 V/nm), a clear band gap forms at the *K* point. For low applied fields, the bands are fairly flat and parabolic near the Fermi energy. However, as the strength of the applied field increases, the band gap continues to grow at the *K* point, while the size of the band gap changes very little at two neighboring shoulders in k space. These shoulders occur at $k_o \approx \pm U/v_f$ from the *K* point, where v_F is the graphene Fermi velocity.[9] The change of the band gap with electric field is illustrated in Fig. 6. The distortion of the bands as the applied electric field increases leads to the characteristic *Mexican hat* band structure shown in Fig. 5(d) that has been discussed in several tight-binding investigations.[8,9] It has also recently been shown in another first-principles calculation that used a different basis set.[10] Similar to the work of Min *et al.*,[10] our calculations indicate

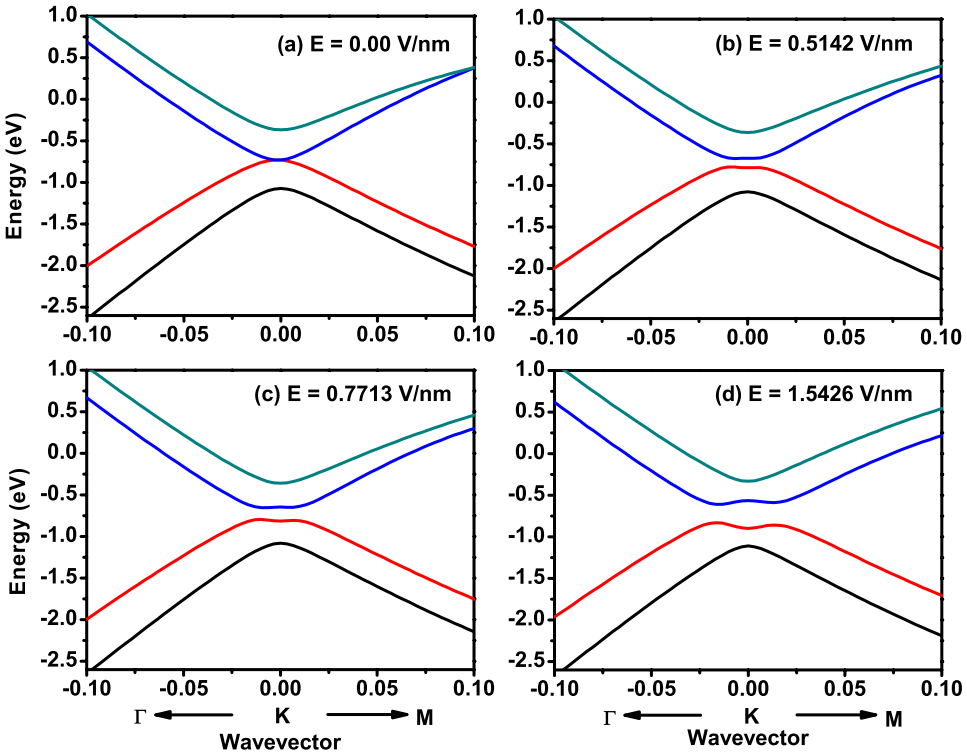

FIG. 5. (Color online) The bands for a bilayer graphene system are shown in the region close to the *K* point for electric fields ranging from 0 to 1.5 V/nm. The *K* point is taken as the origin of the graph and the momentum vector is given in units of $2\pi/a$. The left and right band directions are denoted by the arrows pointing toward the high symmetry k points, Γ and *X*, respectively, which are outside of the plotted region.

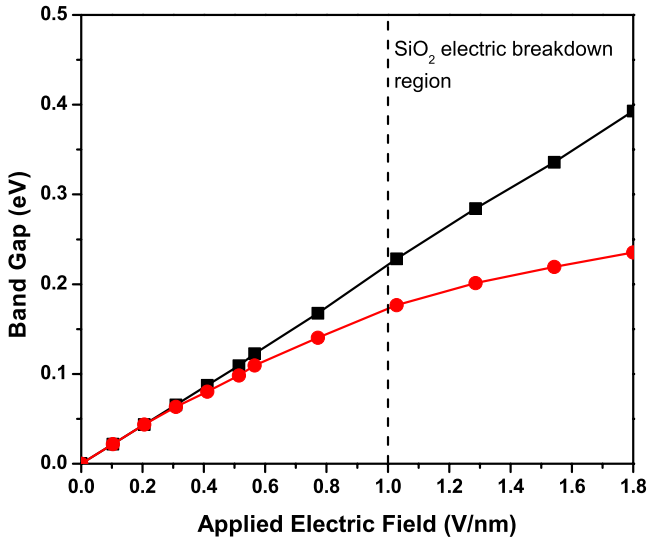

FIG. 6. (Color online) The band gap is shown as a function of the applied field. The black squares denote the band gap measured at the K point. The red circles indicate the band gap measured at the higher shoulders in the band structure near the K point. The field where electric breakdown of SiO_2 occurs is denoted by a vertical dash line and band gap values for higher fields are not achievable in practical devices.

that the band gap saturates to a maximum value of 0.25 eV with applied electric field. Doping a graphene bilayer with potassium on one side, Ohta *et al.*[6] found a maximum band gap of approximately 0.2 eV. For practical device design, it is also important to take into account the electric breakdown of SiO_2, which occurs at approximately 1 V/nm.[26] Based on this constraint, our approach predicts that a band gap of 0.17 eV is feasible.

Cross sections for the induced charge in a bilayer graphene system are shown in Fig. 7 for 0.7713 and 1.5426 V/nm, respectively. The cross sections are perpendicular to the graphene plane and taken along the line defined by the dark gray atoms in Fig. 1. Since the induced charge monotonically increases, the above fields were primarily chosen to highlight the increase in induced charge. In both cases, there is a clear electron charge cloud on the bottom side of the bilayer graphene and a significant positive charge cloud on the opposite side of the bilayer. It is also important to note that the induced charge concentration on the B sites is significantly greater than on the neighboring A sites. As expected, as the electric field increased, the induced charge increased on both the A and B sites. The higher charge concentration on the B sites was observed in the induced charge distribution for all applied fields considered.

In order to get a better understanding of the induced charge distribution, we added the effects of applied electric fields to a previous tight-binding Green's function model for bilayer graphene.[27] The model consists of nearest neighboring coupling of $\gamma_1=3.0$ eV and $\gamma_2=0.4$ eV between A sites in adjacent graphene layers. The on-site energy ε for the case of graphene is zero. The applied electric field induces potentials U_1 and U_2 in the first and second layers, respectively. The Hamiltonian in this case is given by

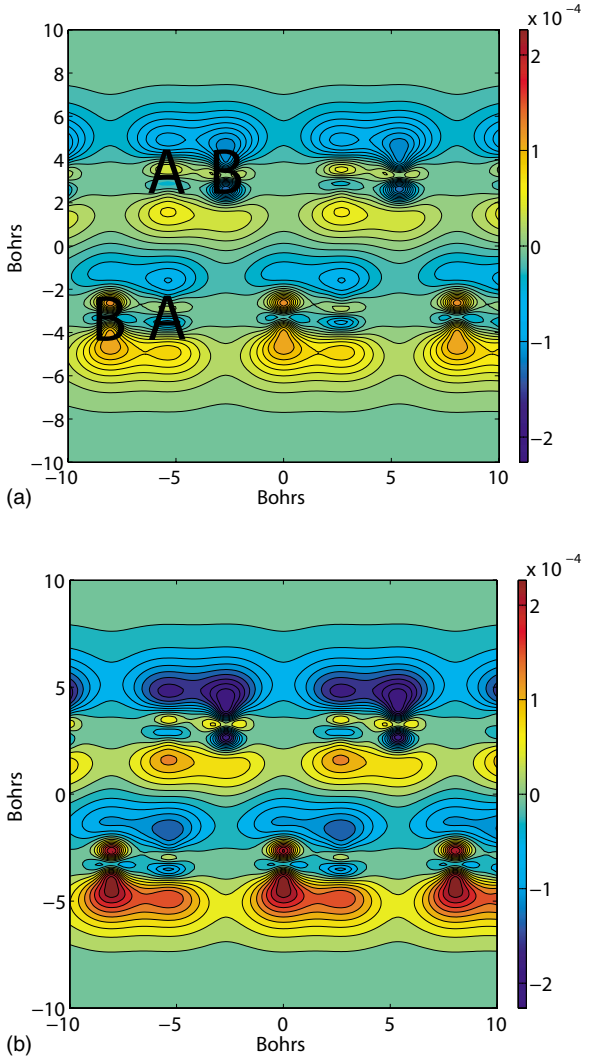

FIG. 7. (Color online) Induced charge in xz plane through the graphene bilayer for (a) 0.7713 V/nm and (b) 1.5426 V/nm. The position of A and B sublattice carbon atoms is denoted for representative atoms in panel (a).

$$H=\begin{bmatrix} \varepsilon-U_1 & \gamma_1\mu^* & \gamma_2 & 0 \\ \gamma_1\mu & \varepsilon-U_1 & 0 & 0 \\ \gamma_2 & 0 & \varepsilon-U_2 & \gamma_1\mu \\ 0 & 0 & \gamma_1\mu^* & \varepsilon-U_2 \end{bmatrix}, \tag{4}$$

where $\mu=e^{ik_ya}+e^{i(-\sqrt{3}ak_x/2-ak_y/2)}+e^{i(\sqrt{3}ak_x/2-ak_y/2)}$.

The Green's function for a bilayer of graphene for a given energy, E, and wavevector, $\mathbf{k}$, are given by $G^R(E,k_x,k_y)=(E-H+i\delta)^{-1}$, where δ is an infinitesimal imaginary component to the energy. The total charge at a given site α in the bilayer can be expressed in terms of the Green's function as

$$\sigma_\alpha=\frac{A^2}{4\pi^2}\int_{-\infty}^{E_f}dE\int_{BZ}d\mathbf{k}\left(\frac{-1}{\pi}\right)\mathrm{Im}\,G^R_{\alpha\alpha}(E,\mathbf{k}), \tag{5}$$

where $A=3\sqrt{3}a^2/2$ is the area of the graphene unit cell in real space. The energy integration can be efficiently performed by using a semicircle in the complex plane that starts

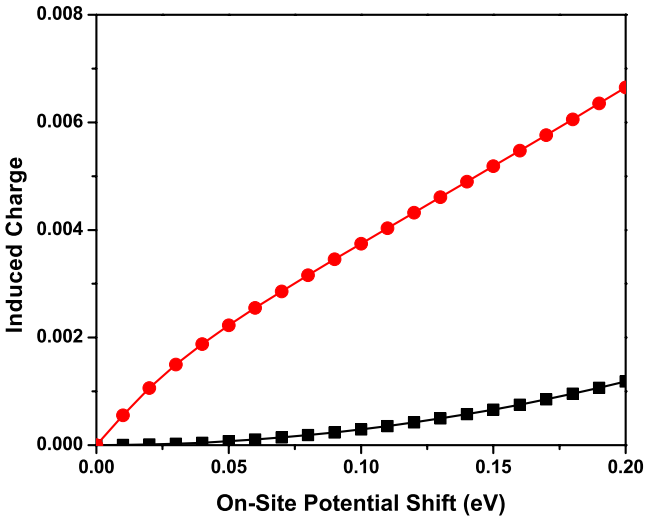

FIG. 8. (Color online) Induced charge predicted by a tight-binding model for the *A* sites (black squares) and *B* sites (red circles) in the top layer of bilayer graphene for different on-site potential shifts.

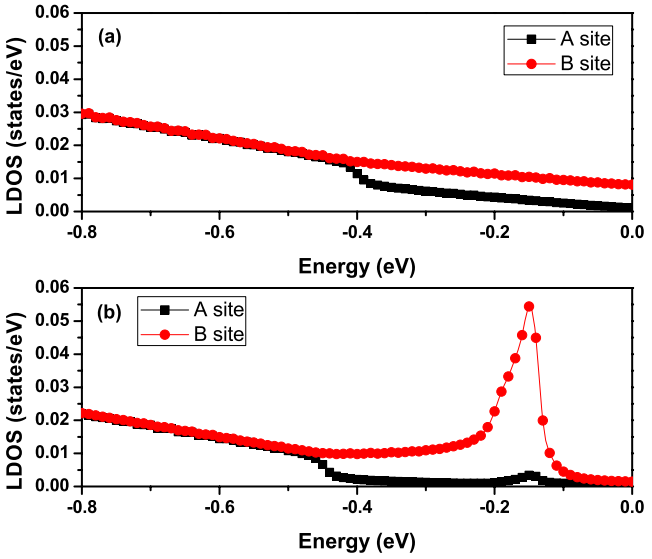

FIG. 9. (Color online) Local density of states for *A* and *B* atoms in layer 1 of a graphene bilayer calculated with the tight binding model (a) with no applied field and (b) with potential shifts $U_1=0.2$ eV and $U_2=-0.2$ eV.

below the valence band.[28] This model provides a bilayer band structure consistent with previous works,[8,9] exhibiting the formation of a band gap with applied field and the characteristic *Mexican hat* band structure near the *K* point.

By using this tight-binding model, we examined the induced charge on the *A* and *B* sites in the top layer of graphene for a range of on-site potential shifts (Fig. 8). The tight-binding model indicates that the induced charge on the *B* site increases very rapidly with the applied field. The induced charge on the *A* sites by contrast shows a small induced charge even for very high on-site potential shifts. Based on this analysis, the tight-binding model predicts that charge will primarily be induced on the *B* sites in the bilayer graphene systems. This corresponds well with what we have observed in our first-principles calculations.

The high degree of induced charge on the *B* sites can be understood by looking at the local density of states. Examining the local density of states (LDOS) at the *A* and *B* sites in each graphene layer with no applied field [Fig. 9(a)], we find that the *B* sites have a significant density of states at the Fermi energy, while the LDOS on the *A* site drops at $E=-\gamma_2$ and is negligible at the Fermi energy. This indicates that the valence band at the Fermi energy is primarily composed of wave functions on the *B* site lattice, while the wave functions on the *A* sites are shifted to lower energies due to the interlayer interactions between neighboring *A* sites. Applied fields will affect the bands closest to the Fermi energy level, which indicates that the electric field will induce charge initially on the *B* sites in the graphene levels.

We considered the case where the first graphene layer had a potential shift of $U_1=0.2$ eV and the second layer had a potential shift $U_2=-0.2$ eV. The local density of states for the *A* and *B* sites in the first layer is shown in Fig. 9(b). There is a clear indication of a van Hove singularity in the density of states at $E=-0.149$ eV on the *B* site atoms. At this same energy, there is also a much smaller peak in the local density of states at the *A* atom site. The peak at the *A* site is most likely due to weak coupling with the *B* sites. The van Hove singularity in the local density of states at the *B* site leads to a high weighting of the density of states at the band edge. This will also lead to a high induced charge. Very high fields are required to create a similar situation at the *A* sites.

This analysis indicates that the tight-binding model is able to explain the charge distribution observed in our density functional calculations. The preferential charging of the *B* sublattice sites could be important in determining possible bonding sites for atomic or molecular absorbants. The fact that an applied electric field will induce a greater charge on the *B* sites could affect the stability of molecules bonded on bilayer graphene.

IV. CONCLUSION

In this study, we have used first-principles approaches and tight-binding techniques to examine the effect of applied electric fields on charge distributions in graphene thin films. The polarizability for different graphene thin films was calculated from first principles and showed a clear linear relationship with the number of graphene layers. Based on these calculations, we determined a bulk dielectric constant for graphite of 3.328 for fields applied along the *c* axis. The surface polarizability for graphene thin films was found to be 0.061 $Å^3$, which is an order of magnitude less than comparable benzene thin films.

The induced charge distribution for bilayer graphene under an applied field was also considered in detail. Our first-principles calculations demonstrated the characteristic *Mexican hat* band structure found in previous tight-binding models.[8,9] Similar to a previous study,[10] we found that the band gap saturated at 0.25 eV with applied field. Due to the electric breakdown of SiO_2 at 1 V/nm, a band gap of 0.17 eV

is feasible in actual bilayer graphene devices. In addition, analysis of the induced charge along the z direction also indicated that screening increased with the number of graphene layers in the structure.

Inspection of the charge distribution from first-principles calculations indicated that for applied fields, the induced charge was primarily located on the B sites in bilayer graphene. We also used a tight-binding Green function model to examine the induced charge on both sites. The tight-binding model also indicates that the B sites should have the greatest induced charge for all applied fields. This preferential charging of B sites could impact the stability of atoms and molecules absorbed on bilayer graphene under applied electric fields.

ACKNOWLEDGMENTS

Calculations were performed on the Intel Cluster at the Cornell Nanoscale Facility which is part of the National Nanotechnology Infrastructure Network (NNIN) funded by the National Science Foundation (NSF). E.K.Y. gratefully acknowledges the support of the Cornell Engineering Learning Initiatives program and the Cornell Center for Nanoscale Systems.

*eky2@cornell.edu
†stewart@cnf.cornell.edu

[1] M. P. Anantram and F. Léonard, Rep. Prog. Phys. **69**, 507 (2006).
[2] K. S. Novoselov, A. K. Geim, S. V. Morozov, D. Jiang, Y. Zhang, S. V. Dubonos, I. V. Grigorieva, and A. A. Firsov, Science **306**, 666 (2004).
[3] C. Berger *et al.*, J. Phys. Chem. **108**, 19912 (2004).
[4] A. K. Geim and K. S. Novoselov, Nat. Mater. **6**, 183 (2007).
[5] S. V. Morozov, K. S. Novoselov, M. I. Katsnelson, F. Schedin, D. C. Elias, J. A. Jaszczak, and A. K. Geim, Phys. Rev. Lett. **100**, 016602 (2008).
[6] T. Ohta, A. Bostwick, T. Seyller, K. Horn, and E. Rotenberg, Science **313**, 951 (2006).
[7] A. Charrier, A. Coati, and T. Argunova, J. Appl. Phys. **92**, 2479 (2002).
[8] E. McCann, Phys. Rev. B **74**, 161403(R) (2006).
[9] F. Guinea, A. H. Castro Neto, and N. M. R. Peres, Phys. Rev. B **73**, 245426 (2006).
[10] H. Min, B. Sahu, S. K. Banerjee, and A. H. MacDonald, Phys. Rev. B **75**, 155115 (2007).
[11] X. Gonze *et al.*, Comput. Mater. Sci. **25**, 478 (2002).
[12] X. Gonze *et al.*, Z. Kristallogr. **220**, 558 (2005).
[13] http://www.abinit.org/Psps/?text=../Psps/LDA_TM/lda
[14] M. C. Schabel and J. L. Martins, Phys. Rev. B **46**, 7185 (1992).
[15] L. A. Girifalco and M. Hodak, Phys. Rev. B **65**, 125404 (2002).
[16] H. Rydberg, N. Jacobson, S. I. Simak, B. I. Lundqvist, and D. C. Langreth, Surf. Sci. **532-535**, 606 (2003).
[17] N. Mounet and N. Marzari, Phys. Rev. B **71**, 205214 (2005).
[18] E. Konstantinova, S. O. Dantas, and P. M. V. B. Barone, Phys. Rev. B **74**, 035417 (2006).
[19] R. D. King-Smith and D. Vanderbilt, Phys. Rev. B **47**, 1651 (1993).
[20] R. W. Nunes and X. Gonze, Phys. Rev. B **63**, 155107 (2001).
[21] I. Souza, J. Iniguez, and D. Vanderbilt, Phys. Rev. Lett. **89**, 117602 (2002).
[22] J. Tóbik and A. D. Corso, J. Chem. Phys. **120**, 9934 (2004).
[23] B. Kozinsky and N. Marzari, Phys. Rev. Lett. **96**, 166801 (2006).
[24] L. Wirtz, M. Lazzeri, F. Mauri, and A. Rubio, Phys. Rev. B **71**, 241402(R) (2005).
[25] R. Resta, Rev. Mod. Phys. **66**, 899 (1994).
[26] D. J. DiMaria, E. Cartier, and D. Arnold, J. Appl. Phys. **73**, 3367 (1993).
[27] Z. F. Wang, Q. Li, H. Su, X. Wang, Q. W. Shi, J. Chen, J. Yang, and J. G. Hou, Phys. Rev. B **75**, 085424 (2007).
[28] I. Turek, V. Drchal, J. Kudrnovsky, M. Sob, and P. Weinberger, *Electronic Structure of Disordered Alloys, Surfaces, and Interfaces* (Kluwer, Dordrecht, 1997).